Journal of Optics

PAPER • **OPEN ACCESS**

Measuring spatial coherence of quantum and classical light with an ultrastable monolithic interferometer

To cite this article: Edoardo Suerra *et al* 2026 *J. Opt.* **28** 015602

IOP Publishing *J. Opt.* **28** (2026) 015602 https://doi.org/10.1088/2040-8986/ae2935

Journal of Optics

OPEN ACCESS

RECEIVED
14 August 2025

REVISED
20 November 2025

ACCEPTED FOR PUBLICATION
8 December 2025

PUBLISHED
19 December 2025

PAPER

Measuring spatial coherence of quantum and classical light with an ultrastable monolithic interferometer

Edoardo Suerra[1,2,*], Mirko Siano[1,2], Bruno Paroli[1,2], Samuele Altilia[1,2], Marco A C Potenza[1,2], Matteo G A Paris[1,2] and Simone Cialdi[1,2]

[1] Dipartimento di Fisica, Università di Milano, I-20133 Milan, Italy
[2] Istituto Nazionale di Fisica Nucleare, Sezione di Milano, I-20133 Milan, Italy
[*] Author to whom any correspondence should be addressed.

E-mail: edoardo.suerra@unimi.it

Keywords: spatial coherence, parametric down conversion, monolithic interferometer

Abstract

We describe a monolithic interferometer for spatial coherence measurements of both classical and quantum light sources. The design enables measurements on both a PDC-based quantum source and a classical thermal source, using two identical calcite crystals to control beam alignment via birefringence. The monolithic structure ensures inherent stability. Spatial coherence is measured through temporal interferograms and spectral analysis, with both methods showing close agreement with theoretical predictions. The system is robust and performs reliably for both quantum and classical light. Its design enables automated, rapid coherence measurements across different source types.

1. Introduction

Spatial coherence is a fundamental property of both classical and non-classical light [1–4]. It describes the ability of an electromagnetic field to maintain a fixed phase relation between different points across the beam profile [2], and is traditionally quantified through the visibility of interference fringes in a Young's double-slit experiment [4, 5]. From a classical perspective, spatial coherence is of utmost importance in many research areas and applications, ranging from high-resolution optical microscopy [6] to wavefront sensing [7], from coherent methods in the x-ray sciences [8, 9] to free-space optical communications [10–12]. The coherence properties of the emitted light also carry useful information on the original radiation source, with applications such as measurements of stellar diameters [13] and non-invasive particle beam diagnostics [14]. Spatial coherence becomes even more significant in the quantum regime, where it underpins remarkable phenomena such as quantum superposition and entanglement. In this context, the coherence properties of light are not merely classical features, but essential resources for quantum technologies, enabling groundbreaking advancements in quantum information, metrology, and imaging [15–17]. In particular, spatial optical correlations play a crucial role in quantum imaging [18] and super-resolution [19], offering new possibilities for metrology, positioning, and high-precision measurements. A striking example is their potential to surpass classical measurement limits; for instance, leveraging the spatial quantum correlations of spontaneous parametric down-conversion (SPDC) emission to detect weak objects could drive significant practical progress [15].

For these reasons, the characterization of spatial coherence—both in quantum and classical regimes—is of paramount importance, and robust and straightforward methods for measuring the spatial coherence of a source are highly desirable. From the quantum perspective, the spatial properties of light—particularly those of twin photons—were investigated as early as the first experimental observation of parametric down-conversion by Burnham and Weinberg [20], who noted that intensity correlations were stronger for specific combinations of detection angles. Subsequent experiments, such as those exploring double-slit interference using twin photons and coincidence counting [21, 22], further elucidated these spatial correlations, with later studies providing more detailed analyses [23, 24]. Additional methodologies, including modified Michelson interferometers [25, 26], have also been explored. Numerous approaches have been proposed also for determining the spatial coherence of classical light, including techniques based on Young's interferometer [27, 28], wavefront folding and shearing interferometers [29–32], random speckle patterns [33–36], gratings [37], plasmonic devices [38], reversed-wavefront interferometers [39], digital micromirror devices [40], among others [41]. Typically, one of the main challenges in experimentally detecting and investigating quantum light lies in the intrinsically low power of quantum states, which often renders them nearly undetectable. As a result, studying their spatial properties, for instance, by translating duplicate copies of the same beam, becomes experimentally impractical. This necessitates the use of intrinsically aligned and highly stable detection systems.

In this work, we introduce an interferometric technique based on a monolithic interferometer to measure the spatial coherence of both quantum and classical light sources. The proposed device, which incorporates two calcite crystals, features an inherently ultrastable design that enables precise control over both spatial and temporal beam overlap. Its monolithic architecture ensures intrinsic alignment throughout the measurement process. We demonstrate the effectiveness of this approach by characterizing the spatial coherence of two distinct light sources: a twin-photon source generated via SPDC and a classical thermal source with a longitudinal coherence length on the order of $1\,\mu$m. The measured transverse coherence lengths are in excellent agreement with theoretical predictions, highlighting the robustness and accuracy of the method. Beyond providing a unified platform for both classical and quantum coherence measurements, this work demonstrates, for the first time to our knowledge, a monolithic spatial-shearing interferometer capable of coincidence-based measurements. Such an intrinsically aligned and ultrastable configuration enables the investigation of spatial correlations in quantum light, whose intrinsically low photon flux makes stability and alignment critical, thereby paving the way for future developments in quantum imaging, sensing, and integrated photonic implementations.

The paper is organized as follows: section 2 describes the experimental setup in detail; section 3 outlines the theoretical framework necessary to describe spatial coherence; section 4 presents the experimental results; finally, section 5 concludes the paper with a discussion of the main findings.

2. Monolithic interferometer and experimental setup

The monolithic interferometer used in this study is illustrated schematically in figure 1. It comprises two identical 40 mm-long calcite crystals and follows the design detailed in [42], itself based on the implementation of [43]. In this work, we use this interferometer for the first time to directly measure the spatial coherence of the optical field. The measurement relies on overlapping distinct transverse portions of the beam, achieved by rotating one of the two birefringent crystals to exploit its birefringence and superimpose two replicas of the same beam, as detailed below. Initially, a beam—either quantum or classical (denoted IN)—is prepared in a horizontal polarization state. A half-wave plate (HWP_1) then rotates this polarization to 45°. The first calcite crystal (C_1) separates the vertical (ordinary) and horizontal (extraordinary) components: the extraordinary ray undergoes a spatial walk-off of $D = 4.18\,$mm upon exiting C_1. A second half-wave plate (HWP_2) subsequently swaps the polarization components before the beams enter the second calcite crystal (C_2). After C_2, the two paths recombine and are projected onto a 45° polarizer (POL), producing an interference pattern. An iris (IRIS) restricts the detection to the desired spatial region. The temporal delay τ between the two arms is controlled by rotating C_1 by a small angle α around its vertical axis (see top view in figure 1). This rotation introduces an additional free-space path $\Delta z = c\tau = D\tan\alpha \approx D\alpha$ for the extraordinary beam, while any alteration of the internal crystal path due to Snell's law is negligible. Similarly, rotating C_2 by a small angle γ around its optical axis induces a vertical shear $\Delta y = D\sin\gamma \approx D\gamma$, with a negligible horizontal shift $\Delta x = D(1-\cos\gamma) \approx 0$. To maintain optimal interference, HWP_2 and POL must be rotated consistently with the orientation of C_2, specifically by $\gamma/2$ and γ, respectively. In this way, transverse spatial coherence can be measured observing the visibility of the interference pattern at the output of the interferometer as a function of the transverse shift. Also, temporal coherence can be measured observing the visibility of the interference pattern at the output of the interferometer as a function of the temporal delay. The achievable spatial and temporal shifts are limited by the crystal rotation angles: a vertical shift of about 1 mm is obtained for $\gamma \approx 15°$, while α must stay below 10° to keep the beam within the crystal, corresponding to a temporal shift of more than 2 ps.

Figure 2 shows the overall experimental setup for measuring spatial coherence where we implemented our monolothic interferometer, with either quantum or classical light sources. For the quantum configuration (figure 2(a)), photon pairs are produced via type-I SPDC in a 3.00 mm-long BBO crystal, pumped by a continuous-wave laser at 405 nm. The pump beam is spatially filtered to ensure a Gaussian mode within the BBO, yielding signal and idler photons at 810 nm. We tested two pump waists in the

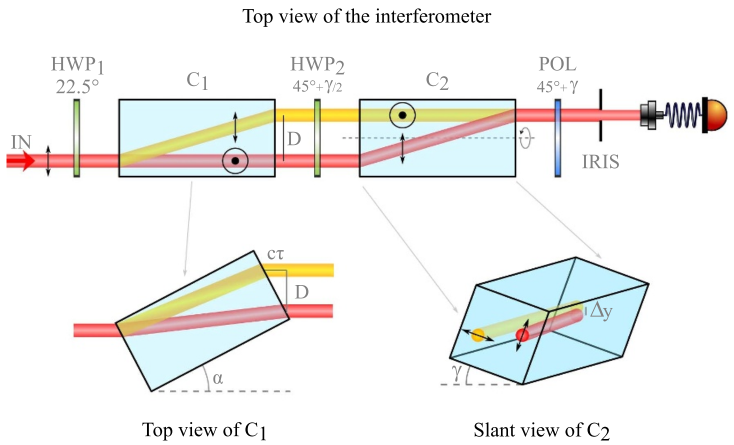

Figure 1. Schematic of the monolithic interferometer (top) and detailed views of the calcite crystals (bottom). IN: input beam; HWP$_i$: half-wave plates; C$_i$: calcite crystals; POL: polarizer; IRIS: iris diaphragm. Rotation of C$_1$ by α introduces a time delay τ, while rotation of C$_2$ by γ produces a vertical displacement Δy.

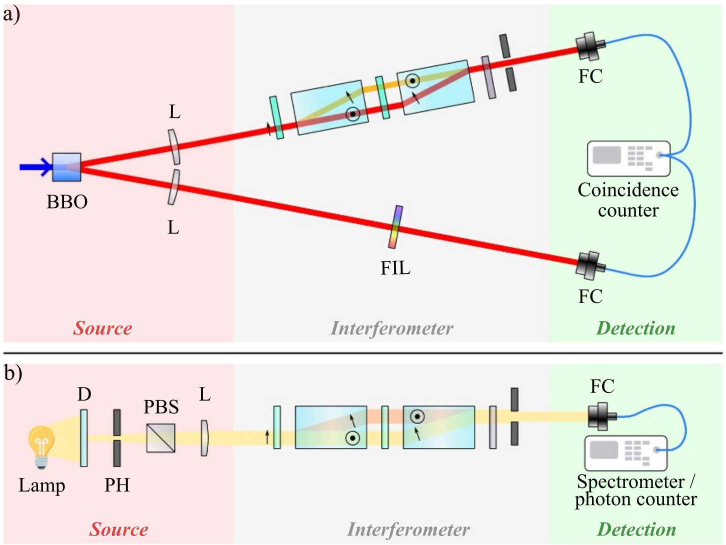

Figure 2. Layout of the coherence measurement apparatus using (a) quantum radiation generated by type-I spontaneous parametric down-conversion (SPDC) in a 3.00 mm-long beta-Barium Borate (BBO) crystal, and (b) a classical thermal source. Acronyms: BBO, beta-Barium Borate; L, lens; FC, single-mode fiber coupler; D, diffuser; PH, pinhole; PBS, polarizing beam-splitter.

crystal of 560 μm and 840 μm. The idler photon is collimated by a 500 mm-focal-length lens and detected by a single-photon counter, while the signal photon follows an identical collimation before entering the interferometer. An electronic timing circuit records coincidence events between signal and idler detectors.

In the classical arrangement (figure 2(b)), a halogen lamp provides broadband light which is diffused by a ground-glass plate, spatially filtered through a 1 mm-diameter iris, and horizontally polarized by a polarizing beam splitter. The resulting beam, centered at $\lambda_0 = 680$ nm with a spectral bandwidth $\Delta\lambda = 150$ nm (FWHM), has an estimated longitudinal coherence length $\lambda_0^2/\Delta\lambda \approx 3\,\mu$m. After collimation by a 500 mm-focal-length lens, the beam enters our monolithic interferometer. The spatially and temporally sheared replicas are either analyzed spectrally using a spectrometer—enabling direct determination of spatial coherence as detailed in section 3—or detected with a photon counter to extract both spatial and temporal coherence from interferograms. A computer controls two stepper motors used for C$_1$ and C$_2$ rotation, and acquires data automatically. The rotation of the polarizing optics is controlled with a precision of fractions of degree.

3. Theoretical model

This section presents a theoretical analysis of the spatial coherence properties of both the quantum and classical sources used in our experiment. We begin by examining the spatial correlations of light generated through SPDC, specifically focusing on type-I SPDC, which is the process employed in our setup.

At the output of the nonlinear crystal, the two-photon quantum state can be written, up to multiplicative constants, in the well-known form [44]:

$$|\psi\rangle = \int \mathrm{d}\omega\, \mathrm{d}^2\vec{k}_s\, \mathrm{d}^2\vec{k}_i\, \tilde{A}_p\left(k_x, k_y\right)\, \mathrm{sinc}\left(\frac{L}{2}\Delta k_z\right) \left|\vec{k}_s, \omega\right\rangle_s \left|\vec{k}_i, -\omega\right\rangle_i , \tag{1}$$

where a monochromatic pump field is assumed. Here, p, s, and i refer to the pump, signal, and idler beams, respectively. The transverse components of the wavevectors are denoted as $\vec{k}_j = (k_{x,j}, k_{y,j})$, and ω represents the angular frequency detuning of the down-converted photons relative to the central angular frequency $\omega_0 = \omega_p/2$. Moreover, $\tilde{A}_p$ is the Fourier transform of the pump field amplitude, and $\Delta k_z = k_{z,p} - k_{z,s} - k_{z,i}$ is the longitudinal phase mismatch. The sinc term originates from the phase-matching function integrated over the crystal length L. In our configuration, this function is sufficiently broad that it can be approximated as unity. Assuming a Gaussian pump beam with beam waist w_p, its angular spectrum is given by:

$$\tilde{A}_p\left(k_x, k_y\right) = \mathrm{e}^{-\frac{w_p^2 |\Delta\vec{k}_\perp|^2}{4}} = \mathrm{e}^{-\frac{w_p^2 \Delta\vec{k}^2_{\perp,x}}{4}}\, \mathrm{e}^{-\frac{w_p^2 \Delta\vec{k}^2_{\perp,y}}{4}} = \tilde{A}_{p,x}\tilde{A}_{p,y} , \tag{2}$$

where $\Delta\vec{k}_\perp = \vec{k}_s + \vec{k}_i$ is the total transverse momentum mismatch. Substituting this expression into the quantum state, we obtain:

$$|\psi\rangle = \int \mathrm{d}\omega\, \mathrm{d}^2\vec{k}_s\, \mathrm{d}^2\vec{k}_i\, \tilde{A}_{p,x}\tilde{A}_{p,y} \left|\vec{k}_s, \omega\right\rangle_s \left|\vec{k}_i, -\omega\right\rangle_i . \tag{3}$$

We now consider the effect of two identical lenses, each of focal length f, used to collimate the signal and idler beams. Each lens maps the transverse momentum $\vec{k}_\perp$ to a transverse spatial coordinate $\vec{r}$ via the relation $\Delta\vec{k}_\perp = \frac{2\pi}{\lambda f}\Delta\vec{r}$. After this transformation, the state becomes:

$$|\psi\rangle = \int \mathrm{d}\omega\, \mathrm{d}x\, \mathrm{d}y\, \tilde{A}_{p,x}\tilde{A}_{p,y} \left|x_s, y_s, \omega\right\rangle_s \left|x_i, y_i, -\omega\right\rangle_i . \tag{4}$$

As discussed in section 2, our interferometric setup superposes two copies of the quantum state along the vertical (y) direction. We can therefore restrict our analysis to this coordinate. At the output of the interferometer, the state undergoes both a vertical displacement Δy and a temporal delay τ, followed by projection through a polarizer that allows the two components to interfere. The resulting state at the detector is given by:

$$|\psi\rangle = \frac{1}{2}\int \mathrm{d}\omega\, \mathrm{d}y\, \tilde{G} \left|y_s, \omega\right\rangle_s \left|y_i, -\omega\right\rangle_i , \tag{5}$$

where

$$\tilde{G} = \tilde{A}_{p,y}(y_s - y_i) + \tilde{A}_{p,y}(y_s - y_i - \Delta y)\, \mathrm{e}^{\mathrm{i}\,\tau(\omega_0 + \omega)} . \tag{6}$$

The coincidence detection probability is obtained by projecting this state onto position and frequency eigenstates:

$$P(\tau, \Delta y) = \int \mathrm{d}\omega'\, \mathrm{d}y_s'\, \mathrm{d}y_i'\, \left|{}_s\langle y_s', \omega'|_i\langle y_i', -\omega'|\psi\rangle\right|^2 = \frac{1}{2} + \frac{1}{2} g(\Delta y)\cos(\omega_0\tau) . \tag{7}$$

Here, the function

$$g(\Delta y) = \int \mathrm{d}y_s\, \mathrm{d}y_i\, \tilde{A}_p(y_s - y_i)\, \tilde{A}_p(y_s - y_i - \Delta y) \tag{8}$$

describes the spatial correlations between the photons. The $\cos(\omega_0\tau)$ term gives rise to interference fringes, and the visibility of these fringes is determined by $g(\Delta y)$. Therefore, the measurement of interference visibility—specifically the dependence on the vertical shift Δy-provides direct information about the spatial coherence and correlations in the photon pairs.

Although the approximation of the sinc to unity is fully adequate under our experimental conditions, where the sinc width (≈10 mm FWHM) largely exceeds the introduced spatial shifts (≈0.5 mm), it is worth noting that for longer crystals or smaller pump waists the sinc term would introduce multiplicative factors inside the integral of equation (8), leading to a reduced transverse coherence length. Such a change would simply modify the coherence function measured by the interferometer, without affecting the operation of the device.

From the classical point of view, let us consider a thermal source of diameter D, as schematized in figure 2(b). The thermal light is linearly polarized and collimated with a lens of focal length f, then it is directed into our interferometer. As for the quantum counterpart, two copies of the beam are overlapped with a temporal shift τ and a spatial (vertical) translation Δy. In the end, the radiation can be coupled either to a spectrometer or a photon counter. Considering the spectrometer, the resulting spectrum is given by

$$S(\lambda) = S_0(\lambda)\left[1 + \mu(\Delta y)\cos\left(\frac{2\pi c\tau}{\lambda}\right)\right], \tag{9}$$

where interference fringes due to the temporal shift τ are modulated by a visibility that depends on the spatial shift Δy, which we can identify as the spatial coherence of the radiation. Thus, by measuring the fringes visibility in the spectrum, one can retrieve the coherence function μ of the source. For the sake of simplicity, let us consider a circular source of radius r, whose coherence function at distance f is given by [2]

$$\mu_{\text{circ}}(\Delta y, \lambda) = 2\left|\frac{J_1\left(\frac{2\pi r}{f\lambda}\Delta y\right)}{\frac{2\pi r}{f\lambda}\Delta y}\right|, \tag{10}$$

being $J_1(z)$ the Bessel function of the first kind. This is the coherence function of our circular source after collimation [2]. By measuring fringes visibility in the spectrum, one can retrieve information about source shape. Since μ, and thus visibility, depends on the wavelength λ, a more accurate analysis can be done by considering the reduced coordinate $\Delta\tilde{y} = \Delta y/\lambda$. This simply gives a spectrum

$$\tilde{S}(\Delta\tilde{y}) = 1 + \mu(\Delta\tilde{y})\cos\left(\frac{2\pi c\tau}{\Delta y}\Delta\tilde{y}\right), \tag{11}$$

and, in case of a circular source, a coherence function

$$\mu_{\text{circ}}(\Delta\tilde{y}) = 2\left|\frac{J_1\left(\frac{2\pi r}{f}\Delta\tilde{y}\right)}{\frac{2\pi r}{f}\Delta\tilde{y}}\right|, \tag{12}$$

from which one can retrieve information about source geometry (i.e. radius). If we consider the photon counter instead of the spectrometer, we can acquire interferograms by varying τ. The normalized intensity pattern of the interferogram can be written as [2]

$$I(\tau, \Delta y) = 1 + \mu_T(\tau)\,\mu_S(\Delta y)\cos\left(\frac{2\pi c}{\lambda_0}\tau + \phi(\Delta y)\right), \tag{13}$$

where $\mu_T(\tau)$ and $\mu_S(\Delta y)$ are the temporal and spatial coherence functions, respectively.

It is important to highlight the effect of beam divergence on spatial coherence measurements, emphasizing the crucial role of beam collimation in the implementation of this method. Let us consider a spherical wavefront with a radius of curvature R at the entrance of the first crystal, C_1. Under the paraxial approximation, the two-crystal interferometer produces straight interference fringes at the detection plane with a periodicity given by $\Lambda = \frac{\lambda}{\Delta y}(R + d)$, where d is the optical distance between the entrance of C_1 and the detector. Defining Φ as the diameter of the collection aperture of the detector, the impact of the interference fringes on spatial coherence measurements becomes negligible when $\Lambda > \Phi$. Conversely, if this condition is not met, the visibility of the interferograms or spectra will be affected. As an example, for typical experimental parameters such as $\Delta y_{\text{max}} = 1\,\text{mm}$, $\Phi_{\text{max}} = 2\,\text{mm}$, $\lambda = 700\,\text{nm}$, and $d = 100\,\text{mm}$, the constraint $R > 2.7$ m must be satisfied. This requirement must be fulfilled by introducing a collimation lens to ensure a well-collimated source, as implemented in our setup.

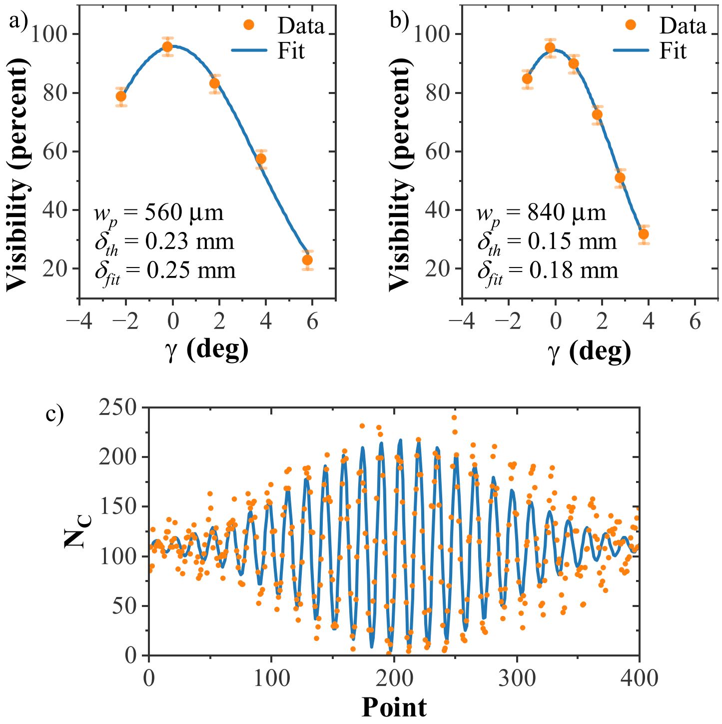

Figure 3. Maximum visibility of the interferograms as a function of spatial displacement Δy for the quantum source from PDC, and for two different pump dimensions of 560 μm (a), and 840 μm (b). In (c) we show an example of an interferogram on the coincidence photon countings N_C, where orange points represents experimental data, while the blue line is their fit.

4. Results

Here we present the results obtained for the quantum and the classical source. Figures 3(a) and (b) reports the measurements of the fringe visibility in the coincidence photon counting as a function of the vertical separation of the states in the interferometer. Orange points are the experimental data, while the blue line is a fit with the theoretical function given by $g(\Delta y)$ of equation (8). In figure 3(a) the pump size is 560 μm (beam radius w), giving a spatial coherence length of 250 μm. The theoretical value of 230 μm is calculated simply by $\delta = \frac{\lambda_0 f}{\pi w}$, and it is in good agreement with the value retrieved by the fit. Here, δ represents the transverse correlation length expected after propagation through the collimation lens of focal length f [45]. Notice that the expression for δ refers to the incoherent field of the SPDC radiation, not to the pump. In figure 3(b) the pump size is 840 μm, corresponding to a spatial coherence length of 180 μm, again in good agreement with the theoretical value of 150 μm. Note that in these measurements dark counts are negligible. The theoretical value is probably underestimated due to uncertainties of lens focal length and beam size. These results demonstrate that this method can be successfully implemented for measurements of spatial correlations of a quantum source. Figure 3(c) shows an example of an interferogram of the coincidence photon countings, with a vertical shift of 40 μm. Here, orange dots are experimental data, while the blue line is a fit with equation (7).

As far as the classical thermal source is concerned, figure 4 shows an example of measurement with the spectrometer. In this example, a vertical shift $\Delta y = 40\,\mu$m is introduced with the crystal C_2, while a temporal delay of $\tau = 93$ fs is introduced with the crystal C_1, giving rise to fringes. In this case, we first demodulated the measured spectrum with respect to the source spectrum, in order to isolate the interference modulation. The visibility of the demodulated spectrum was 92.6%. We performed acquisitions with a fixed temporal delay of 93 fs and for different values of Δy, then, we calculate the spectrum in reduced coordinates $\Delta\tilde{y} = \Delta y/\lambda$ and aggregate data. Results are shown in figure 5. Following equation (11), the envelope of this trend is given by $\mu(\Delta\tilde{y})$. Assuming a circular shape of the source, we retrieve information about source size using equation (12), in particular the radius r, and, consequently, the diameter. We performed measurements for different diameters of the interferometer iris (1.0 mm (a), 1.5 mm (b), and 2.0 mm (c)). In the three cases, we obtained a value of the diameter of 1.15 mm ± 0.01 mm, 0.973 mm ± 0.005 mm, and 0.975 mm ± 0.004 mm, respectively, compatible with the nominal value of 1.00 mm. Here, the errors are retrieved from the uncertainties of the fit parameters. The greater discrepancy of the first case is due to a lower signal on the spectrometer caused by the smaller

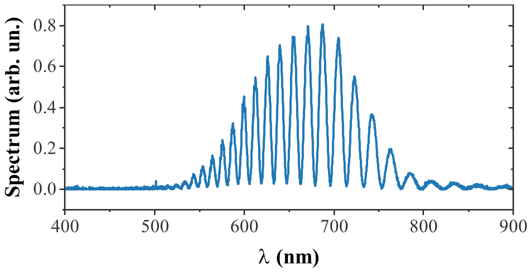

Figure 4. Example of measurement of the spectrum of classical thermal source, with a temporal delay of $\tau = 93$ fs.

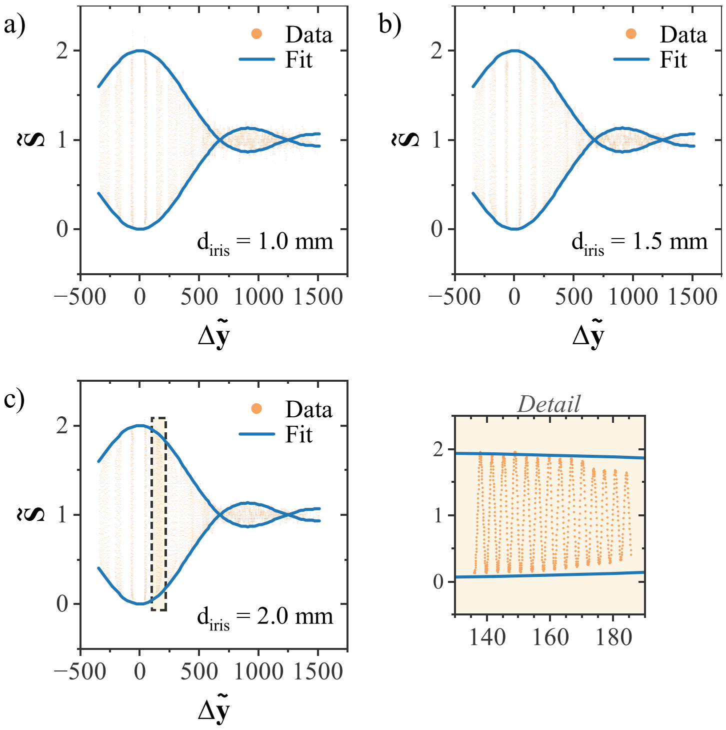

Figure 5. Results from classical thermal source, for different iris diameters of 1.0 mm (a), 1.5 mm (b). and 2.0 mm (c). The fit with the theoretical function gives a value of the source diameter of 1.15 mm, 0.97 mm, and 0.97 mm, respectively, compatible with the nominal value of 1.00 mm. In (c) a detail of the measured reduced spectrum is shown on the right (detail from dashed box).

iris aperture after the interferometer, so that zeroes of the Bessel function are noisy. Notice that in the fit, we fixed the value of the focal length of the lens to 500 mm. These results confirm that the method is robust.

A final measurement with classical light is acquiring interferograms instead of spectra. In this part, the radiation after the interferometer is sent to a photon counter. Acting on C_1, we measured the intensity on the detector with the photon counter as a function of τ, obtaining fringes in the temporal domain. Once spatial shift Δy is fixed, their envelope is directly related to the temporal coherence of our source, while a constant factor is related to spatial coherence, according to equation (13) Thus, by measuring the maximum visibility of each interferogram as a function of Δy, we could retrieve the spatial coherence function $\mu_S(\Delta y, \lambda)$ of equation (13). Results are reported in figure 6, for different iris diameters of the interferometer of 1.0 mm, 1.5 mm, and 2.0 mm. Assuming again a circular shape of the source, i.e. $\mu_S(\Delta y) = \mu_{\mathrm{circ}}(\Delta y, \lambda_0)$ (see equation (12)), being λ_0 the central wavelength of the radiation, we retrieve the source dimension of 1.00 mm±0.01 mm for each of the three cases, where uncertainties are retrieved from the fit parameters and propagated. These measurements are in good agreement with the nominal value of the source diameter of 1 mm for each iris aperture. In the classical regime, both spectral and interferogram measurements were performed to cross-validate the method and to illustrate two alternative approaches for retrieving spatial coherence information using the same interferometer.

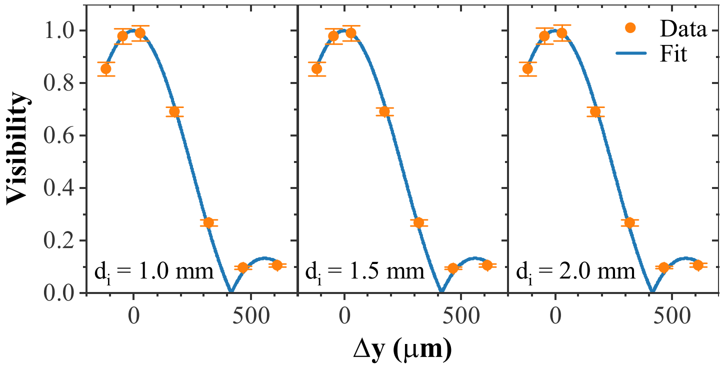

Figure 6. Results from interferograms of the classical thermal source. The fit with the theoretical function gives a value of the source diameter of 1.00 mm ± 0.01 mm for each of the three cases, compatible with the nominal value of 1.00 mm.

5. Conclusions

We have demonstrated a monolithic interferometer for spatial coherence measurements that operates effectively across both quantum and classical optical regimes. The device, based on two identical calcite crystals, successfully characterized spatial coherence properties of SPDC photon pairs and classical thermal light from a halogen lamp. For the quantum source, measured spatial coherence lengths of 180 μm and 250 μm for pump waists of 840 μm and 560 μm respectively showed excellent agreement with theoretical predictions. Similarly, for the classical source, extracted diameters of 0.997–1.15 mm across different iris settings matched the nominal 1.00 mm pinhole size, confirming the method's accuracy.

The monolithic architecture provides inherent stability through rigid optical alignment, eliminating common experimental challenges associated with mechanical drift and thermal fluctuations. This design enables precise control of both temporal delays (via rotation angle α of crystal C_1) and spatial shearing (via angle γ of crystal C_2) without requiring active stabilization systems. The interferometer's dual-mode detection capability, supporting both spectral analysis and coincidence counting, makes it possible to cross-validate measurements and ensures broad applicability to diverse light sources.

Our technique provides a unified platform for quantum–classical coherence characterization, bridging traditionally separate experimental domains. Additionally, the automated, computer-controlled implementation enables rapid measurements previously unattainable with conventional interferometers. Finally, the theoretical framework developed for SPDC correlations and thermal source coherence shows remarkable consistency with experimental data.

Our scheme may have applications in quantum imaging and sensing technologies where spatial coherence underpins performance limits. It may also offer practical utility in beam diagnostics for particle accelerators and astronomical instrumentation. Future research directions include extending the technique to pulsed sources, integrating the interferometer with integrated photonic circuits for miniaturization, and exploring spatiotemporal coherence coupling in complex light fields. The robust design principles demonstrated here may further enable adaptations for UV or x-ray coherence measurements using alternative birefringent materials.

Data availability statement

All data that support the findings of this study are included within the article (and any supplementary files).

Acknowledgment

This work has been supported by Istituto Nazionale di Fisica Nucleare, Group V, with the project ADAMANT.

ORCID iDs

Edoardo Suerra 0000-0002-5695-698X
Mirko Siano 0000-0002-9818-2863

Bruno Paroli 0000-0002-9314-1982
Marco A C Potenza 0000-0002-9379-6540
Matteo G A Paris 0000-0001-7523-7289
Simone Cialdi 0000-0002-2733-927X

References

[1] Loudon R 1980 *Rep. Prog. Phys.* **43** 913–49
[2] Goodman J W 1985 *Statistical Optics / Joseph W. Goodman* (Wiley)
[3] Allevi A, Jedrkiewicz O, Brambilla E, Gatti A, Peřina J, Haderka O and Bondani M 2014 *Phys. Rev. A* **90** 063812
[4] Mandel L and Wolf E 1995 *Optical Coherence and Quantum Optics* (Cambridge University Press) (available at: www.cambridge.org/core/product/identifier/9781139644105/type/book)
[5] Young T 1804 *Phil. Trans. R. Soc.* **94** 1–16
[6] Aguirre A D, Zhou C, Lee H C, Ahsen O O and Fujimoto J G 2015 *Optical Coherence Microscopy* (Springer) pp 865–911
[7] Paroli B, Siano M and Potenza M A C 2018 *Europhys. Lett.* **122** 44001
[8] Nugent K A 2010 *Adv. Phys.* **59** 1–99
[9] Chapman H N and Nugent K A 2010 *Nat. Photon.* **4** 833–9
[10] Paroli B, Siano M and Potenza M A C 2021 *Opt. Express* **29** 14412–24
[11] Paroli B, Cremonesi L, Siano M and Potenza M 2022 *Opt. Commun.* **524** 128808
[12] Horst Y *et al* 2023 *Light: Sci. Appl.* **12** 153
[13] Michelson A A and Pease F G 1921 *Astrophys. J.* **53** 249–59
[14] Siano M *et al* 2022 *Phys. Rev. Accelerators Beams* **25** 052801
[15] Brida G, Genovese M and Ruo Berchera I 2010 *Nat. Photon.* **4** 227–30
[16] Pittman T B, Shih Y H, Strekalov D V and Sergienko A V 1995 *Phys. Rev. A* **52** R3429–32
[17] Tan S H, Erkmen B I, Giovannetti V, Guha S, Lloyd S, Maccone L, Pirandola S and Shapiro J H 2008 *Phys. Rev. Lett.* **101** 253601
[18] Lugiato L A, Gatti A and Brambilla E 2002 *J. Opt. B: Quantum Semiclass. Opt.* **4** S176–83
[19] Boto A N, Kok P, Abrams D S, Braunstein S L, Williams C P and Dowling J P 2000 *Phys. Rev. Lett.* **85** 2733–6
[20] Burnham D C and Weinberg D L 1970 *Phys. Rev. Lett.* **25** 84–87
[21] Ribeiro P H S, Pádua S, Machado da Silva J C and Barbosa G A 1994 *Phys. Rev. A* **49** 4176–9
[22] Strekalov D V, Sergienko A V, Klyshko D N and Shih Y H 1995 *Phys. Rev. Lett.* **74** 3600–3
[23] Fonseca E J S, Monken C H, Pádua S and Barbosa G A 1999 *Phys. Rev. A* **59** 1608–14
[24] Walborn S, Monken C, Pádua S and Souto Ribeiro P 2010 *Phys. Rep.* **495** 87–139
[25] Cutipa P, Spasibko K Y and Chekhova M V 2020 *Opt. Lett.* **45** 3581
[26] Kwon O, Ra Y S and Kim Y H 2009 *Opt. Express* **17** 13059
[27] Partanen H, Friberg A T, Setälä T and Turunen J 2019 *Photon. Res.* **7** 669
[28] Saastamoinen K, Leppänen L P, Vartiainen I, Friberg A T and Setälä T 2018 *Optica* **5** 67
[29] He Q, Turunen J and Friberg A T 1988 *Opt. Commun.* **67** 245–50
[30] Wessely H W and Bolstad J O 1970 *J. Opt. Soc. Am.* **60** 678
[31] Breckinridge J B 1972 *Appl. Opt.* **11** 2996_1–8
[32] Arimoto H and Ohtsuka Y 1997 *Opt. Lett.* **22** 958
[33] Alaimo M D, Potenza M A C, Manfredda M, Geloni G, Sztucki M, Narayanan T and Giglio M 2009 *Phys. Rev. Lett.* **103** 194805
[34] Kashyap Y, Wang H and Sawhney K 2015 *Phys. Rev. A* **92** 033842
[35] Gutt C *et al* 2012 *Phys. Rev. Lett.* **108** 024801
[36] Siano M, Paroli B and Potenza M A C 2021 *Adv. Phys. X* **6** 1891001
[37] Pfeiffer F, Bunk O, Schulze-Briese C, Diaz A, Weitkamp T, David C, van der Veen J F, Vartanyants I and Robinson I K 2005 *Phys. Rev. Lett.* **94** 164801
[38] Morrill D, Li D and Pacifici D 2016 *Nat. Photon.* **10** 681–7
[39] Santarsiero M and Borghi R 2006 *Opt. Lett.* **31** 861
[40] Partanen H, Turunen J and Tervo J 2014 *Opt. Lett.* **39** 1034
[41] Turunen J, Halder A, Koivurova M and Setälä T 2022 *J. Opt. Soc. Am. A* **39** 214–39
[42] Cialdi S, Suerra E, Altilia S, Olivares S, Paroli B, Potenza M A C, Siano M and Paris M G A 2024 *Phys. Rev. A* **110** 043701
[43] Siano M, Paroli B, Cialdi S, Olivares S, Paris M G A, Suerra E and Potenza M A C 2024 *Opt. Commun.* **557** 130349
[44] Schneeloch J and Howell J C 2016 *J. Opt.* **18** 053501
[45] Saleh B E A and Teich M C 1991 *Fundamentals of Photonics* (Wiley) (available at: https://onlinelibrary.wiley.com/doi/book/10.1002/0471213748)